Oxide Sensor Measurements and Simultaneous Optical Observations During Dissolution of Alumina in Cryolite Melt

Luis Bracamonte, Kristian Etienne Einarsrud, Christian Rosenkilde, and Espen Sandnes

Abstract

Faster dissolution of alumina is one of the key challenges for improvement of the energy efficiency and production rate increase of Hall-Héroult electrolysis cells. To obtain a faster dissolution, a better knowledge of the phenomena involved in the alumina dissolution process becomes important. In this work, an alumina sensor based on the electromotive force principle was applied to measure the concentration of dissolved alumina in a cryolite-based melt from the addition of the alumina throughout the entire dissolution process. Simultaneously, the dissolution process was video recorded. The measurements were performed in a quartz crucible and alumina was added in 1 wt% subsequent additions. Three different industrial aluminas were tested. The general working principle of the sensor was studied, and the information extracted from the video recordings was used to explain the sensor results as well as the general dissolution phenomena. The total dissolution time found based on the sensor results and video recording was compared for different alumina concentrations. The influence of stirring of the melt was also studied.

Keywords

Alumina dissolution • Electrochemical sensor • See-through cell

Introduction

The dissolution of alumina in aluminium reduction cells is a complex process which involves several steps. During the feeding, a crust is formed around the alumina particles when the bath freezes, followed by heating and re-melting of the crust around the alumina particles. Gamma-alumina goes through a phase transition to alpha-alumina which then dissolves [1, 2]. Moreover, the dissolution process is affected by several conditions such as bath composition, bath temperature, and alumina properties, among others. Due to the complexity of the process, a method to perform in situ alumina concentration measurements during the dissolution will lead to information for characterizing the alumina-bath interaction and bring to light the variables that influence the dissolution characteristics and dissolution rate of alumina. This information can be valuable to later improve the industrial alumina feeding and dissolution process. Haverkamp and Thonstad developed methods to measure the concentration of alumina based on electrochemical techniques such as linear sweep voltammetry (LSV), critical current density (CCD), and chronopotentiometry [3–5]. Other researchers have focused on electromotive force (emf), a technique which has been experimented with on lab scale in several molten salt systems [6, 7]. Visual observations have also been used to extract information about the dissolution of alumina. Using transparent cells, Yang et al. studied the raft formation and dissolution rates of different aluminas with known physicochemical properties in cryolite-based melts [8, 9]. The aim of the present work was to create a good basis for extracting detailed information from the dissolution process. Video recordings of the alumina dissolution in a transparent quartz crucible were performed. In the same quartz crucible, a relatively simple emf-based alumina sensor was simultaneously used to follow the amount of dissolved alumina from the addition and throughout the whole dissolution process. The total dissolution time for both techniques was compared. Images from

L. Bracamonte · K. E. Einarsrud · E. Sandnes (✉)
Department of Materials Science and Engineering, Norwegian University of Science and Technology (NTNU), Sem Saelands vei 12, N-7491 Trondheim, Norway
e-mail: espen.sandnes@ntnu.no

C. Rosenkilde
Norsk Hydro ASA, Hydro's Corporate Technology Office, Oslo, Norway

© The Minerals, Metals & Materials Society 2022
D. Eskin (ed.), *Light Metals 2022*, The Minerals, Metals & Materials Series,
https://doi.org/10.1007/978-3-030-92529-1_52

the video recordings lead to a better understanding of the performance of the sensor. Simultaneous images from visual observations and in situ alumina sensor measurements have previously not been reported.

Method

The half-cell reactions for the alumina sensor and a quasi-reference electrode are derived together with the corresponding Nernst equation. The alumina sensor is a graphite electrode immersed in the bath (chamber I). The potential of the sensor is measured against the quasi-reference electrode with an undefined potential. The quasi-reference electrode consists of a graphite electrode immersed in a bath with the same composition as for the sensor but saturated with alumina (chamber II). Thus, the potential between the sensor and the quasi-reference is due to the difference in activity of alumina in the two chambers. The principle of the alumina sensor is shown on the left in Fig. 1.

The half-cell reactions for the alumina sensor and the quasi-reference electrode are shown in Eqs. (1) and (2), respectively. Equation (3) represents the migration of sodium ions from chamber I to chamber II in order to maintain charge neutrality. In Eq. (3), t_{Na+} is assumed equal to 1 [10]. However, the addition of 3.5 wt% LiF in the experiments makes the assumption more uncertain. The reason why LiF was added is explained in the experimental part. The total cell reaction is shown in Eq. (4).

$$\text{Half}-\text{cell rx chamber I } O^{2-}_{(I)} + C_{(I)} = 2e^- + CO_{(I)} \quad (1)$$

$$\text{Half}-\text{cell rx chamber II } CO_{(II)} + 2e^- = C_{(II)} + O^{2-}_{(II)} \quad (2)$$

$$\text{Ionic transport } 2t_{Na^+_{(I)}} = 2t_{Na^+_{(II)}} \quad (3)$$

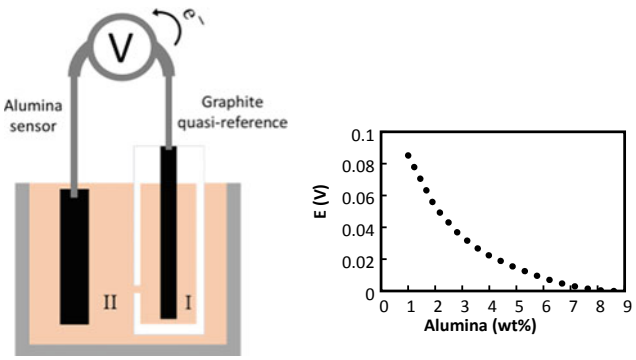

Fig. 1 On the left: schematic of the alumina sensor. On the right: calculated values of the potential of the alumina sensor versus the quasi-reference electrode as a function of alumina concentration (T = 950 °C, the corresponding alumina saturation is 8 wt% $Al_2O_{3(I)}$)

$$\text{Total cell rx } C_{(I)} + CO_{(II)} + Na_2O_{(I)} = CO_{(I)} + C_{(II)} + Na_2O_{(II)} \quad (4)$$

As E^0 is equal to 0, the Nernst equation for the cell reaction becomes as written in Eq. (5), where n is equal to 2.

$$E = -\frac{RT}{nF} \ln \frac{P_{CO_{(I)}} \cdot a_{Na_2O_{(II)}} \cdot a_{C_{(II)}}}{P_{CO_{(II)}} \cdot a_{Na_2O_{(I)}} \cdot a_{C_{(I)}}} \quad (5)$$

The activity of CO is expressed as the partial pressure of CO above the melt since the adsorbed CO is believed to be in equilibrium with dissolved CO which is also in equilibrium with the pressure of CO above the melt. The expression in Eq. (5) can be simplified to Eq. (6) as $a_{C_{(I)}}$ is equal to $a_{C_{(II)}}$ because the same graphite material is used in both electrodes, and with the assumption that the CO pressure is constant and equal in chambers I and II.

$$E = -\frac{RT}{2F} \ln \frac{a_{Na_2O_{(II)}}}{a_{Na_2O_{(I)}}} \quad (6)$$

By using data from FactSage (ThermFact Inc., Montreal, Canada), it can be found that a_{Na_2O} is roughly linearly related to the alumina concentration. This implies that the activity coefficient of Na_2O is approximately constant. Since the bath composition is the same in chambers I and II, Eq. (6) simplifies to Eq. (7).

$$E = -\frac{RT}{2F} \ln \frac{wt\%Al_2O_{3(II)}}{wt\%Al_2O_{3(I)}} \quad (7)$$

Finally, the potential of the alumina sensor can be expressed as a function of the alumina concentration. The calculated values are given on the right of Fig. 1.

Experimental

Design of the Alumina Sensor

The alumina sensor is shown on the left of Fig. 2. The probe is a graphite rod (Ø 1 cm, h 5 cm) shielded with a boron nitride tube on the top. The purpose of the shielding is to hinder the reaction with air possibly present above the melt and to prevent the carbon to be in contact with the crust after feeding. The probe was made of the same graphite material as the graphite rod used for the quasi-reference electrode.

The quasi-reference electrode is based on a graphite rod (Ø 0.5 cm, h 5 cm) which was screwed to a graphite connector and put inside a boron nitride tube ($Ø_{inner}$ 1 cm, $Ø_{outer}$ 2.5 cm). A hole (Ø 0.1 cm) was drilled above the bottom of the tube to ensure ionic contact between the alumina saturated bath inside the tube (chamber I) and the bath in the crucible (chamber II). A stainless-steel rod was screwed to

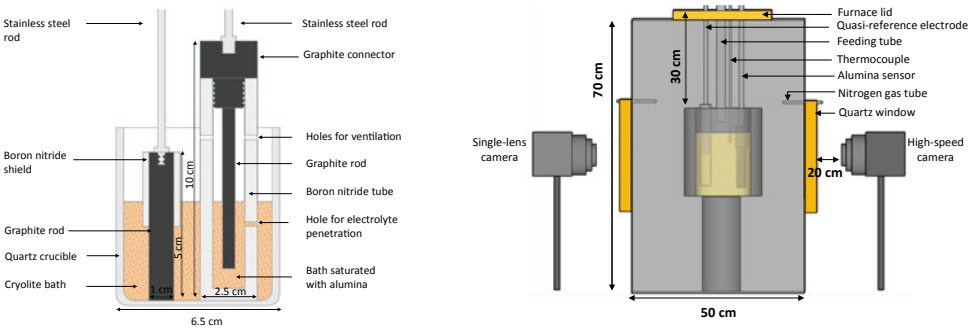

Fig. 2 On the left: sketch of the quartz crucible with the alumina sensor and the quasi-reference electrode. On the right: principal sketch of the see-through furnace. The alumina feeding tube and the thermocouple are also inserted through the lid. The high-speed camera is shown on the right and the single-lens camera on the left

the graphite connector. Alumina powder (2.5 g) was added inside the boron nitride tube to make an alumina saturated bath (approximately 8 wt%).

Electrolyte and Alumina

The experiments were performed using 250 g of bath. The initial composition was synthetic cryolite (74 wt%), aluminium fluoride (15 wt%), calcium fluoride (6.5 wt%), and lithium fluoride (3.5 wt%). The synthetic cryolite contained approximately 1 wt% of alumina. The use of LiF lowered the liquidus point of the bath allowing to operate the furnace at lower temperatures resulting in a longer lifetime of the crucible and materials inside the furnace. For the additions, three different industrial-grade secondary aluminas were used. Some of their physicochemical properties are shown in Table 1.

Experimental Setup and Procedure

The experimental setup is shown on the right of Fig. 2. A transparent quartz crucible (Ø 6.5 cm, h 7.5 cm) was used to contain the bath. The crucible was placed inside a see-through furnace with quartz windows on the sides. The furnace was custom-made from Entech Energiteknik AB. Nitrogen was flushed from both windows (100 mL/min) to prevent vapors and particles from sticking to the windows thereby enhancing the visibility. The furnace was not completely sealed, so the nitrogen gas inside the furnace could contain small amounts of oxygen from the ambient air. A stainless-steel tube (Ø 1.5 cm, h = 30 cm) together with a funnel was used for the additions of alumina. The melt temperature was measured with a thermocouple type S and was kept around 950 °C prior to additions. The theoretical liquidus temperature was around 922 °C given a superheat of approximately 28 °C. The relatively high superheat was necessary to avoid freezing of the bath due to the absence of insulation material and heating elements in the see-through zone. In addition, the effect of convection in the electrolyte was also studied by applying a stainless-steel rod stirrer at a constant rotation speed of 200 rpm. The emf between the alumina probe and the graphite quasi-reference electrode was measured before and during the addition of alumina and throughout the entire dissolution process for all the experiments. A Data Acquisition System (DAQ) measurement hardware (NI 9205) was used for obtaining the emf data.

Simultaneous video recording during the additions and dissolution process of the alumina was performed using a high-speed camera (Photron FASTCAM Mini AX) and a digital single-lens reflex camera (Sony) located in front of the windows of the oven. The images shown in the present work are all taken from the high-speed camera due to its high-quality images suitable for extracting the dissolution characteristics. The high-speed camera could only serve for the first 5 minutes of the dissolution process due to limitations in memory capacity. The digital single-lens reflex camera was used to record the whole dissolution process for each alumina addition and to estimate the dissolution time.

Table 1 Physicochemical characteristics of the different aluminas

Alumina	MOI (300 °C) (%)	LOI undried (1000 °C) (%)	BET surface (m^2/g)	γ-alumina (%)	Particles ≤ 45 µm (%)
A	1.70	2.33	69.8	38.1	15
B	2.65	2.11	65	37.2	10
C	1.50	1.86	73.9	39.7	10

Four subsequent additions of 1 wt% of Alumina A, B, and C were performed. The feeding tube was placed approximately 1 cm above the melt. The time from the first alumina particle hit the surface until the last particle hit was in the range from 0.5 to 1.5 s. The addition is considered as finished when the last particle has hit the melt. The time stamp for pictures later presented refers to the completion of the addition.

Results and Discussion

Interpretation of Sensor Data and Video Recordings

The emf data and the melt temperature for the dissolution of Alumina A are presented in Fig. 3. In general, after each addition the emf curve shows a decrease which is interpreted as an increase in the alumina concentration. Then, the potential stabilizes and reaches more or less a constant value when the dissolution process is closed to completion. For the first addition, the emf curve shows a fast decrease before the potential reached a horizontal plateau suggesting that the dissolution process was completed, while less pronounced drops and slightly inclining plateaus were observed for the subsequent additions.

The time when each alumina addition was performed and the time when the dissolution was estimated to be finished based on the alumina sensor and video recordings are also shown in the figure. Based on the video recordings, the dissolution process was considered to be finished at the moment when no trace of crust or rafts was seen in the bath. This time could be decided with an estimated accuracy of approximately ±0.2 min. The inaccuracy arises from transparency limitations of the crucible in addition to difficulties being able to see small rafts through the meniscus that the melt made on the surface of the quartz crucible walls.

For additions number 2 and 3, the dissolution process has finished before the inclination of the plateau appears. The inclination is therefore assumed to be drifting of the sensor. The cause of the drifting is not understood. In Fig. 3, the green dashed lines show the linear regression lines associated with the drifting occurring from the end of the dissolution process to the next addition. The average of the slope of these two lines is used for the correction of the sensor data in the same time range. This correction is done for addition numbers 2–4 and the corrected values are represented by the red lines. The purpose of the correction is to be able to more accurately estimate the dissolution time based on the sensor data. In the estimation, a horizontal line was drawn from the time when the dissolution was estimated to be completed based on the video recording to the time of the addition. The line is positioned on the plateau value and extended back to the time of the addition. The time when the horizontal line started to deviate from the emf curve was taken as the time when the dissolution was completed. This time could be decided with an estimated accuracy of approximately ±0.4 min. The inaccuracy arises from the fluctuations in the curve making it impossible to define one specific time as the end of the dissolution.

The measured potential values were generally not in agreement with the calculated values for all the aluminas. The difference arises from simplifications done in the deduction of the Nernst equation and the sensitivity of the

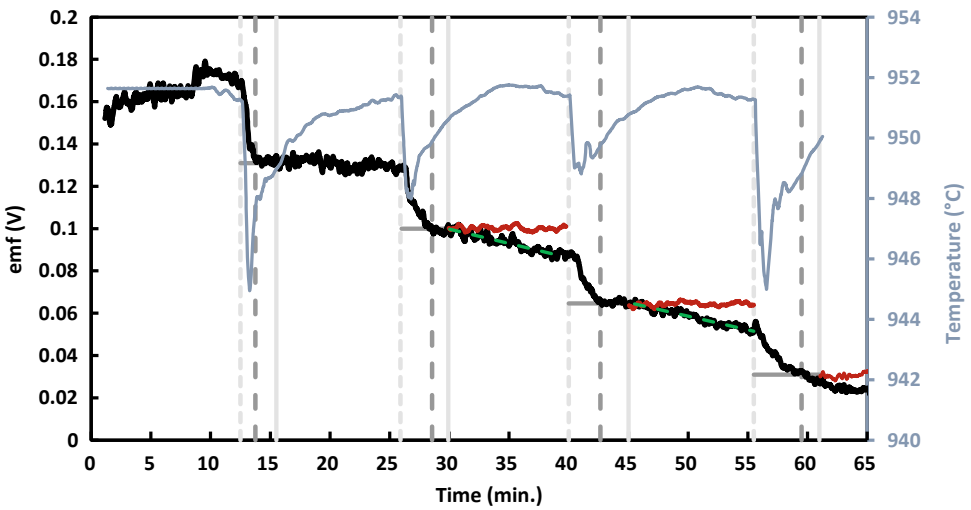

Fig. 3 Emf of the alumina sensor and the melt temperature for additions of Alumina A. Emf (black line). Temperature (blue line). Time of addition (light-grey short dashed line). Time for end of dissolution based on the video recording (light-grey line). Correction of the emf curve (red line). Linear regression line (green dashed line). Line for extension of the plateau (dark-grey solid line). Time for end of dissolution based on the alumina sensor (dark-grey long dashed line) (Color figure online)

sensor to variations of the gas concentration in or above the melt. Despite this difference, the general behaviour of the emf curve after each alumina addition makes it possible to estimate dissolution times, suggesting that the working principle for the sensor is partly confirmed.

Generally, the temperature drops between 2 and 6 °C for the alumina additions were observed. This was comparable with previous studies [11]. The time from feeding until the temperature approaches the temperature before addition showed a slight agreement with the dissolution time based on video recording and sensor measurements, especially for the second and the third addition. Anyway, the relationship is loose, and the temperature data is not used in further analysis.

Figure 4 shows in detail the simultaneous emf measurement and the dissolution characteristics recorded by the high-speed camera for the first addition of Alumina A. Frame (a) shows the situation before feeding. The quasi-reference is located on the left, the alumina sensor is on the right, and the thermocouple Pt and PtRh threads are shown in the middle of the crucible. Upon addition, the alumina penetrated 2 cm into the bath, frame (b). After one second, frame (c), a fraction of the alumina penetrated the bath and rapidly dispersed forming a white cloud which underwent a rapid dissolution a few centimeters down below the surface of the melt. Moreover, the other fraction of the alumina remained on the top of the bath forming a layer or crust with a lot of gas bubbles trapped inside. The bubbles inside the layer had an average size of about 1 mm in diameter. After 20 s, dissolution of the white cloud in the upper part of the crucible was observed, frames (d)–(f). This rapid dissolution is also observed in the fast decrease in the emf curve. Frame (g) shows the situation after 1 min. In a relatively short time, the crust had almost completely dissolved with only a few small rafts of approximately 1 mm in diameter remaining on the surface. At this time, the emf curve is about to reach the plateau value. After 1.3 min, the dissolution process was considered to be finished based on the alumina sensor data, illustrated by the dark-grey dashed line. Almost no alumina particles were left in the crucible after 2.5 min, frame (h). Frame (i) shows a completely transparent bath with no alumina remaining neither in the crucible bottom nor at melt surface. Thus, based on the video recording, the dissolution was considered to be finished after 3 min. In Fig. 4, a lot of bubbles can be seen to have formed on the BN part of the quasi-reference. The origin of these bubbles is uncertain. Periodically the bubbles were released. Frame (h) shows an example of a big bubble being released from the bottom of the BN part. Gas was also evolved on the graphite sensor. The gas evolution might have caused some noise in the emf curves and sometimes sudden convection increase in the bath.

The emf data for the additions of Alumina B is presented on the left of Fig. 5. For the first addition, the emf decreased quickly before reaching an almost constant value. The principal shape of the emf curve resembles the shape of the emf curve for Alumina A, including the drift after the dissolution process has finished. Although not shown, the same principles for correction apply to Fig. 5 as to Fig. 3.

Due to technical problems, the sensor data from the first two addtions of Alumina C could not be obtained. For this reason, the emf curve on the right of Fig. 5 shows addition numbers 3–6. Here, it was possible to estimate the dissolution time only for the third and the fourth addition based on the alumina sensor measurements. Unlike the results obtained for Alumina A and B, the sudden emf drop after each addition was larger for Alumina C. The potential later increased and more or less stabilized forming a plateau. This type of behaviour of the emf can be explained by a lot of alumina ending up close to the sensor during or after feeding, increasing the concentration rapidly in the volume nearby the sensor. Afterwards the alumina concentration around the sensor decreases. The video recordings for Alumina C appear not very different from the video recordings for Alumina A and B, and thus cannot explain the difference in the emf curve.

Figure 6 shows images from the fourth addition of Alumina A, with an initial bath concentration of approximately 4 wt% alumina. Contrary to the first addition, most of the alumina remained on the top of the bath forming a thicker crust with larger gas bubbles trapped inside. The bursting of the bubbles inside promoted the detachment and following sinking of smaller parts of the crust. These parts had flake-like shapes of 2–10 mm length, probably consisting of alumina particles in a bath matrix with density greater than the bath [12]. The whole dissolution process was completed after 5 min evidencing a significantly longer dissolution time. The same phenomenon was also observed for Alumina B and C at this higher initial concentration.

Dissolution Time

A general trend was observed in the dissolution times based on the sensor for Alumina A, B, and C, characterized by decreasing dissolution rate with increasing alumina concentration. This was reflected in the behaviour of the emf curve, with a fast decrease immediately after the first alumina addition and a less pronounced decrease as the initial alumina concentration increased in the subsequent additions. The same trend was observed in the dissolution times based on video recordings. Estimated dissolution times for all the aluminas are given in Table 2 and Fig. 7.

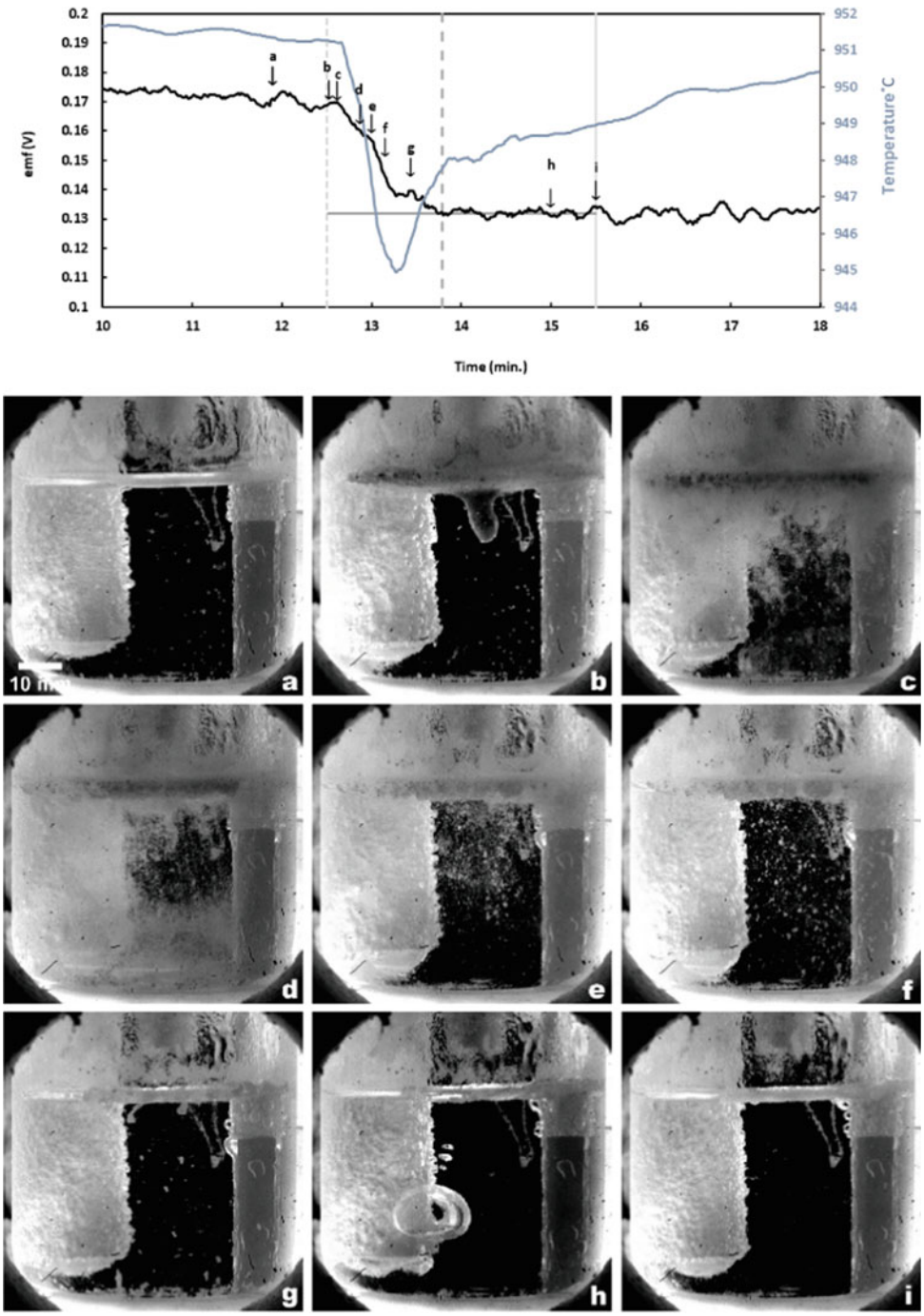

Fig. 4 Simultaneous emf measurements and images from the dissolution process of the first addition of Alumina A **a** before addition **b** upon addition **c** 1 s **d** 20 s **e** 30 s **f** 40 s g 1 min h 2.5 min **i** 3 min

The estimated dissolution times based on the alumina sensor were lower than the estimated times based on the video recordings. The reason for the lower values obtained using the alumina sensor might be related to the method for estimating the dissolution time from the emf curve as the emf curve probably obtained a plateau value before the remaining alumina in the crust was able to dissolve. The difference in the dissolution times based on the alumina sensor and video recordings was especially pronounced at lower initial alumina concentrations probably because a major part of the alumina dissolves quickly, as described in relation to Fig. 4, while at higher initial alumina concentrations more of the alumina ended up in the crust making the dissolution times based on the sensor and video recordings to obtain more similar values. In general, the dissolution times obtained based on the sensor do not show a significant difference between the dissolution times of Alumina A and B. For Alumina C, it is difficult to conclude due

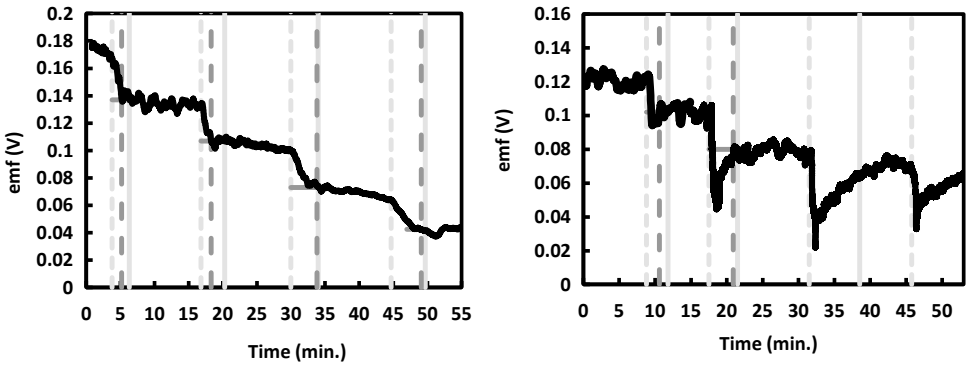

Fig. 5 On the left: emf of the alumina sensor for additions of Alumina B. Emf (black line). On the right: emf of the alumina sensor for additions of Alumina C. Emf (black line). Time of each addition (light-grey short dashed line). Time for end of dissolution based on the video recording (light-grey line). Line for extension of the plateau (dark-grey solid line). Time for end of dissolution based on the alumina sensor (dark-grey long dashed line)

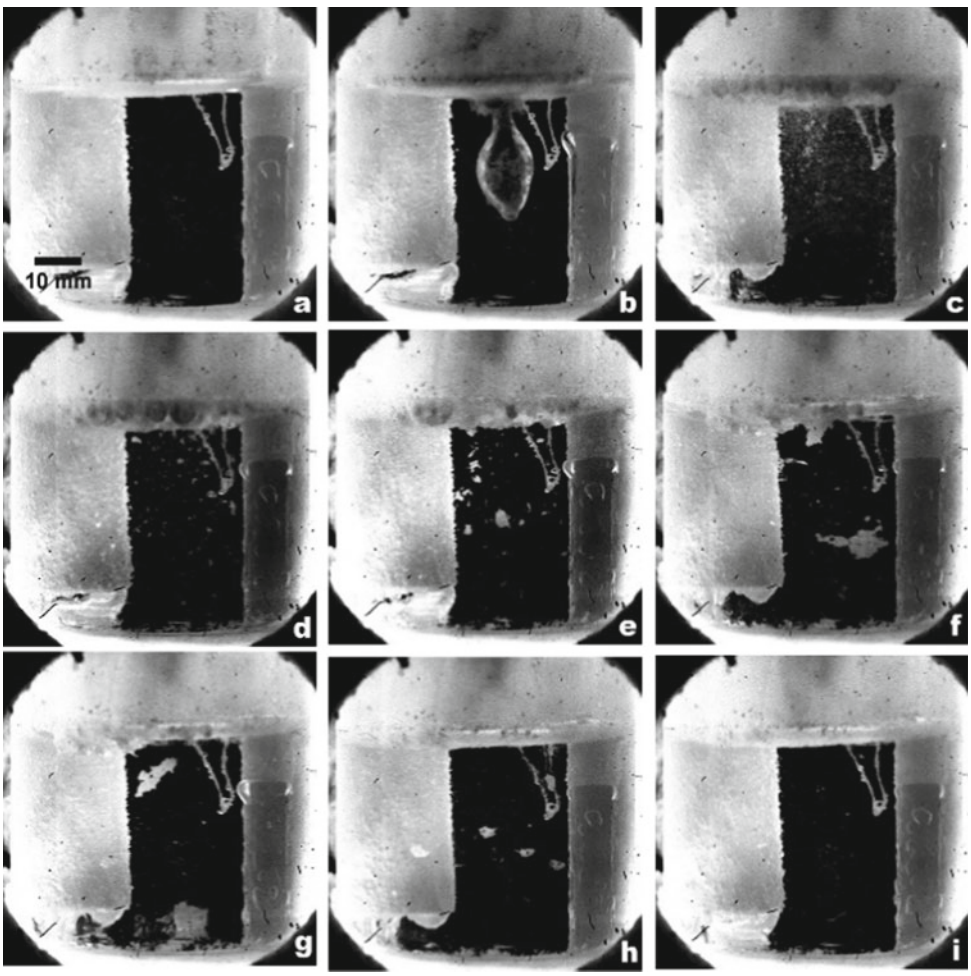

Fig. 6 Selected images for the dissolution process of the fourth addition of Alumina A **a** before addition **b** upon addition **c** 1 s **d** 20 s **e** 30 s **f** 40 s g 80 s h 2.5 min **i** 5 min

to the lack of measurements. On the other hand, the video recordings together with the described method to estimate the dissolution time indicate a significant difference in the dissolution times of the aluminas with respect to complete dissolution of the crust. The shorter dissolution times based on video recordings for Alumina C might be related to some physicochemical properties as its highest BET surface and lowest content of particles ≤ 45 µm among the three aluminas. These properties are usually related to fast dissolution rates [9]. However, it is difficult to conclude because

Table 2 Dissolution times of the aluminas based on the alumina sensor and video recordings

Alumina	Alumina addition number	Dissolution time (min)	
		Alumina sensor (±0.4)	Video recording (±0.2)
A	1	1.3	3.0
	2	2.6	4.0
	3	2.7	5.0
	4	4.5	5.5
B	1	1.4	2.5
	2	1.9	3.5
	3	3.8	4.0
	4	4.4	5.0
C	1	Not measured	2.0
	2	Not measured	3.0
	3	1.8	3.0
	4	3.4	4.0

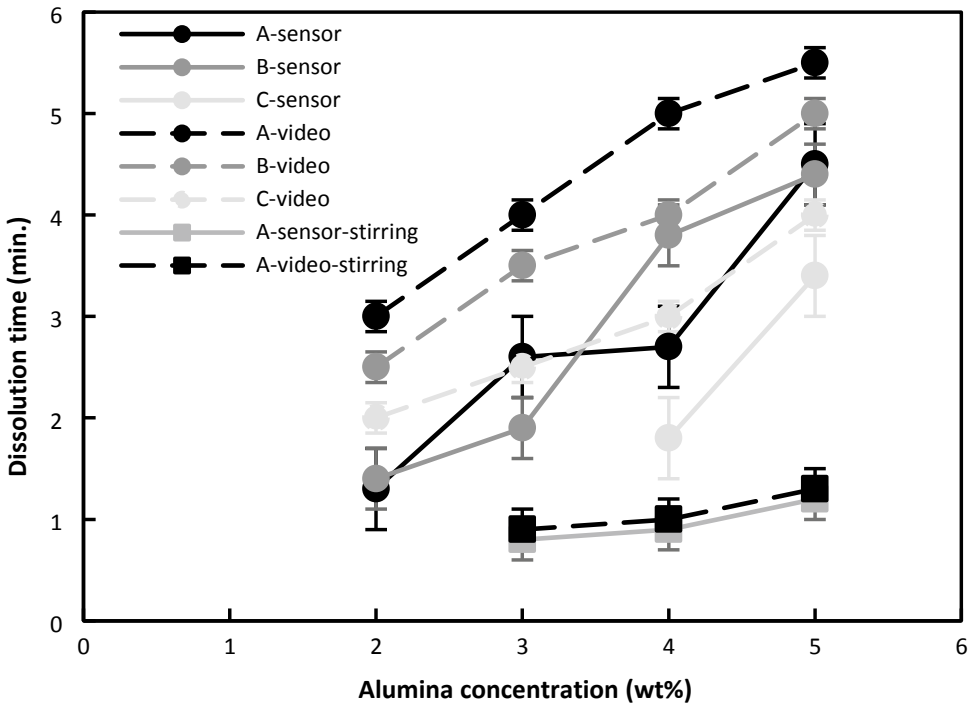

Fig. 7 Dissolution times of the aluminas without stirring based on the alumina sensor (solid line with circles) and video recordings (dashed lines with circles). Dissolution times for Alumina A with stirring based on the alumina sensor (solid line with squares) and video recordings (dashed lines with squares)

Alumina C also has the lowest LOI and MOI values among the aluminas, also properties related to fast dissolution rates.

Based on emf measurements, Yasinskiy et al. [13] reported alumina dissolution times between 3.7 and 6 min for subsequent 1 wt% alumina additions in a KF-AlF_3-Al_2O_3 melt at 750 °C. These dissolution times are slightly higher than for the present work, but this can be explained by the lower temperature.

Influence of Stirring on the Alumina Dissolution

The obtained emf curve when stirring was applied is shown in Fig. 8. The most significant differences compared to the experiments without stirring are a faster decrease in emf immediately after feeding and shorter time to reach the plateau values. For all additions, a horizontal plateau was reached. The mechanical stirring promoted a rapid

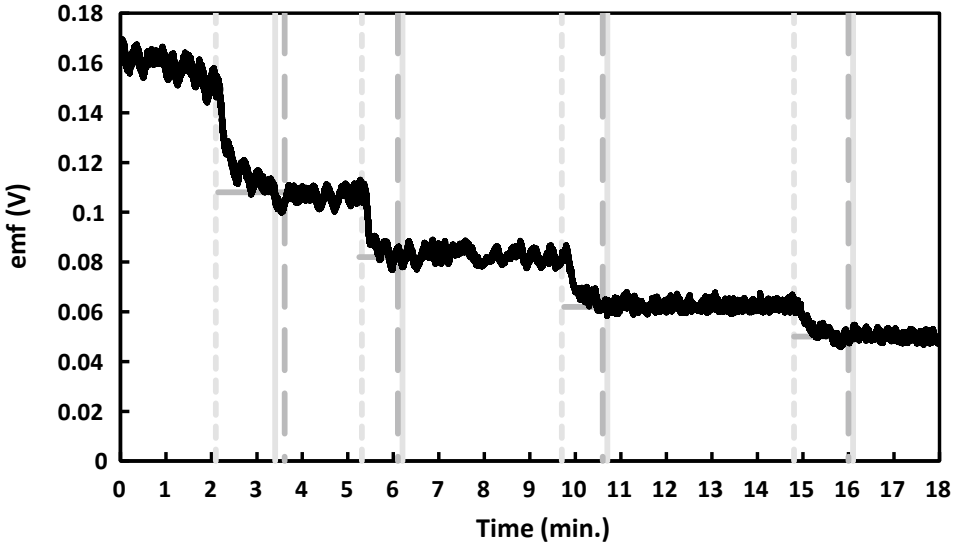

Fig. 8 Emf of the alumina sensor for additions of Alumina A when mechanical stirring was applied (black line). Time of each addition (light-grey short dashed line). Time for end of dissolution based on the video recording (light-grey line). Line for extension of the plateau (dark-grey solid line). Time for end of dissolution based on the alumina sensor (dark-grey long dashed line)

Table 3 Dissolution times for Alumina A based on the alumina sensor and video recordings when stirring was applied

Alumina addition number	Dissolution time (min)	
	Alumina sensor (±0.2)	Video recording (±0.2)
1	1.5	1.4
2	0.8	0.9
3	0.9	1.0
4	1.2	1.3

dispersion giving a faster dissolution of the alumina particles in the cryolite melt and possibly also to a large degree reducing crust formation. These observations agree with the results found by Yang [14]. The estimated dissolution times based on the video recordings and the alumina sensor are given in Table 3. These results suggest that the dissolution process is mainly limited by mass transport as reported by Haverkamp and Welch [15].

Figure 9 shows the images for the first addition and dissolution process of Alumina A when stirring was applied. Upon addition, the alumina very rapidly dispersed in the bath, and 1 s after addition was finished a 5 mm thick crust formed with bubbles less than 1 mm in diameter trapped inside it, frame (c). After 2 s, the particles started to detach from the crust and rapidly dissolved before reaching the bottom of the crucible, frame (d). Later, frames (e–f), the bubbles inside the crust reached maximum size with average diameters of around 3 mm before bursting. At this time, part of the crust was already dissolved. The whole dissolution process was completed after approximately 1.4 min, frame (i).

When excluding the dissolution time obtained for the first addition due to technical problems with the stirrer for this addition, smaller deviation in the dissolution times based on the alumina sensor and video recordings were found, Table 3 and Fig. 7. This can be explained by the reduced crust formation. Also, the increased convection from stirring has made the dissolution time less affected by the initial alumina concentration.

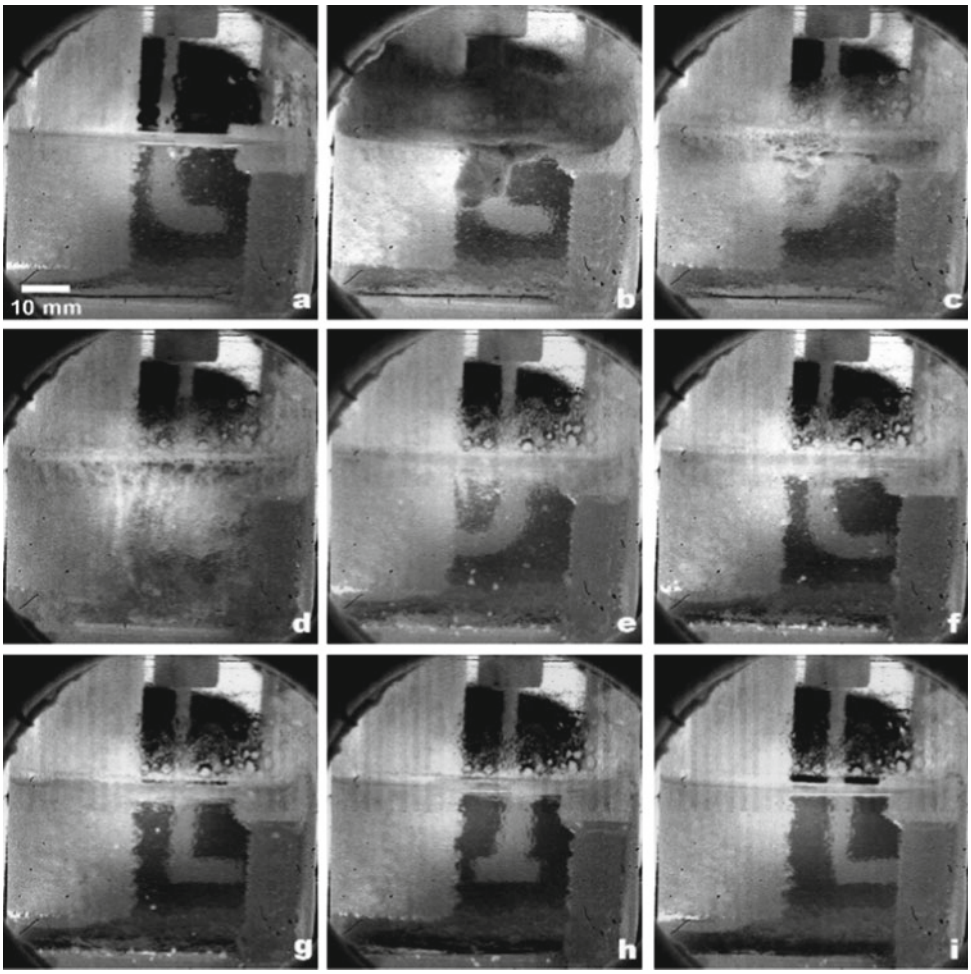

Fig. 9 Selected images for the dissolution process of the first addition of Alumina A when mechanical stirring was applied. **a** before addition **b** upon addition **c** 1 s **d** 2 s **e** 6 s **f** 30 s g 45 s h 1 min **i** 1.4 min

Conclusion

The emf curve obtained using the alumina sensor made it possible to estimate the dissolution times of the aluminas based on the initial decrease in emf immediately after alumina addition and the plateau value reached when most of the alumina was dissolved. The working principle for the sensor was only partly confirmed as the actual potential values were generally not in agreement with the calculated values. The video recordings revealed a rapid dispersion of the alumina immediately after addition. At lower alumina concentration, a thin crust formed but the dissolution is mainly proceeding through the dissolution of a white cloud consisting of smaller dispersed alumina particles. The crust became thicker the higher the initial alumina concentration in the melt and it dissolved mainly by detachment and sinking of flake-shaped particles. The estimated dissolution times based on the alumina sensor and video recordings show an increase in the dissolution time with increasing initial alumina concentration. Introduction of convection by stirring the melt resulted in smaller dissolution times by reducing the amount of crust formation.

Acknowledgements This work is partially funded by SFI Metal Production, Centre for Research-based Innovation, 237738. Financial support from the Research Council of Norway and the partners of SFI Metal Production are gratefully acknowledged.

References

1. Lavoie P, Taylor M, Metson J (2016) A review of alumina feeding and dissolution factors in aluminium reduction cells. Metallurgical and Materials Transactions B, Vol 47B, 2690–2696.
2. Dassylva-Raymond V, Kiss L, Poncsak S (2014) Modeling the behaviour of alumina agglomerate in the Hall-Héroult process. Light Metals 2014, 603–608. Wiley, Hoboken.
3. Haverkamp RG, Welch BJ (1998) Modelling the dissolution of alumina powder in cryolite. Chemical engineering and processing 37, 177–187.
4. Thonstad J (1967) Critical current densities in cryolite melts. Electrochimical Acta, Vol 12, 1219–1226.
5. Thonstad J (1972) Dissolution of alumina in molten cryolite. Metallurgical Transactions, Vol 3, 408.

6. Vasyunina NV, Vasyunina IP, Mikhalev YG, Vinogradov AM (2009) The solubility and dissolution rate of alumina in acidic cryolite aluminous melts. Russian Journal of Non-Ferrous Metals, 50(4):338–342.
7. Bracamonte L, Nilsen K, Rosenkilde C, Sandnes E (2020) Alumina Concentration Measurements in Cryolite Melts. Light Metals 2020.
8. Yang Y, Gao B, Wang Z, Shi Z, Hu X (2015) Study on the Dissolution of Alumina in Cryolite Electrolyte Using the See-Through Cell. Light Metals 2015.
9. Yang Y, Gao B, Wang Z, Shi Z, Hu X (2015) Effect of Physiochemical Properties and Bath Chemistry on Alumina Dissolution Rate in Cryolite Electrolyte. JOM, Vol 67, No 5.
10. Haarberg GM, Osen KS, Thonstad J (1993) Measurement of electronic conduction in cryolite alumina melts and estimation of its effect on current efficiency. Metallurgical Transactions B. Vol 24B, 729–735.
11. Kuschel G, Welch BJ (1990) Effect of alumina properties and operation of smelting cells on the dissolution behavior of alumina. Pasmico Research Center, Newcastle, Australia. Department Chemical and Material Engineering, University of Auckland, New Zealand.
12. Gylver, S (2019) The micro-and macrostructure of alumina raft. Light Metals 2019, 689–696.
13. Yasinskiy A, Suzdaltsev A, Polyakov P, Padamata S, (2020) Behaviour of aluminium oxide in KF-AlF_3-Al_2O_3 melts and suspensions, Ceramics International.
14. Yang Y, Gao B, Shi Z, Hu X (2015) The Formation and Dissolution of Crust Upon Alumina Addition into Cryolite Electrolyte. JOM. Vol 67. 2170–2180.
15. Haverkamp RG, Welch BJ (1998) Modelling the dissolution alumina powder in cryolite. Chemical Engineering and Processing. Vol 37,177–187.